Earth and Planetary Science Letters 289 (2010) 162–170

Contents lists available at ScienceDirect

Earth and Planetary Science Letters

journal homepage: www.elsevier.com/locate/epsl

Shock and post-shock temperatures in an ice–quartz mixture: implications for melting during planetary impact events

R.G. Kraus [a,*], S.T. Stewart [a], A. Seifter [b], A.W. Obst [b]

[a] Department of Earth and Planetary Sciences, Harvard University, Cambridge, Massachusetts, USA
[b] Los Alamos National Laboratory, Physics Division, Los Alamos, New Mexico, USA

ARTICLE INFO

Article history:
Received 10 July 2009
Received in revised form 23 October 2009
Accepted 2 November 2009
Available online 24 November 2009

Edited by: T. Spohn

Keywords:
shock temperature
impact cratering
melting
water ice
equation of state

ABSTRACT

Melting of H_2O ice during planetary impact events is a widespread phenomenon. On planetary surfaces, ice is often mixed with other materials; yet, at present, the partitioning of energy between the components of a shocked mixture is still an open question in the shock physics community. Knowledge of how much energy is partitioned into the ice component is necessary to predict and interpret a wide range of processes, including shock-induced melting and chemistry. In this work, we construct a conceptual framework for the thermodynamic pathways of the components in a shocked hydrodynamic mixture by defining three broad regimes based on the characteristic length scale of the mixture compared to the thickness of the shock front: (1) small length scale mixtures where pressure and temperature equilibrate immediately behind the shock front; (2) intermediate length scales where pressure but not thermal equilibration is achieved behind the shock front; and (3) long length scales where pressure equilibration requires multiple shock wave reflections. We conduct shock wave experiments, reaching pressures from 8 to 23 GPa, in an H_2O ice–SiO_2 quartz mixture in the intermediate length scale regime. In each experiment, all the parameters required to address the question of energy partitioning were determined: the shock velocity in the mixture, the shock front thickness, and the shock and post-shock temperatures of the H_2O component. The measured pressure is in agreement with the bulk compressibility of the mixture. The shock and post-shock temperatures of the H_2O component indicate that the ice was shocked close to the principal Hugoniot. Therefore, in the intermediate length scale regime, the partitioning of shock energy is defined initially by the Hugoniots of the components at the equilibrated pressure. We discuss energy partitioning in mixtures over the wide range of length and time scales encountered during planetary impact events and identify the current challenges in calculating the volume of melted ice. In some cases, the criteria for shock-induced melting of ice in a mixture are the same as for pure ice.

1. Introduction

Shock-induced melting of H_2O ice during impact cratering events is an important planetary phenomenon. As relatively low shock pressures are required to melt ice (Stewart et al., 2008), large volumes of melt may be produced during impact events. Depending on the size of the event, the liquid water may persist for time scales relevant for prebiotic chemistry (Artemieva and Lunine, 2003; Furukawa et al., 2009). Hence, impact craters may have played a key role in the development of habitable environments (Cockell and Bland, 2005). The generation of liquid water during impact events has been inferred from the distinct morphologies of craters on Mars (Carr et al., 1977) and the Galilean icy satellites (Senft and Stewart, submitted for publication). On Mars, cumulative impact events may have significantly redistributed water contained in near-surface reservoirs (Stewart et al., 2004) and, early in the planet's history, large impacts may have created transiently clement global climatic conditions (Segura et al., 2008; Segura et al., 2002). The amount of liquid water produced by shock melting pure ice during an impact event has been revisited using numerical simulations (Kraus and Stewart, in preparation) that include a revised ice shock Hugoniot (Senft and Stewart, 2008; Stewart and Ahrens, 2005) and new criteria for shock-induced melting (Stewart et al., 2008).

However, on planetary surfaces, H_2O ice is commonly mixed with other materials. For example, ice is mixed with silicates and other refractory materials on the surfaces of Earth, Mars, some icy satellites, and dwarf planets. H_2O ice may also be mixed with other, more volatile ices in bodies in the outer solar system, such as some icy satellites, comets and their parent bodies. Numerical studies of collisions onto such bodies have modeled material mixtures using two different approaches: (1) the mixture is treated as a single material using an averaged equation of state (Pierazzo et al., 2005) and (2) each component is modeled with individual equations of state and the energy partitioning between components is calculated

* Corresponding author. Tel.: +1 617 496 0064.
E-mail address: rkraus@fas.harvard.edu (R.G. Kraus).

0012-821X/$ – see front matter © 2009 Elsevier B.V. All rights reserved.
doi:10.1016/j.epsl.2009.11.002

(Stewart et al., 2004). The former has the advantage of being numerically stable and the disadvantages of significantly simplifying the thermodynamics of icy mixtures and preventing phase separation. The latter approach allows for phase separation and retains the thermodynamic properties of individual phases but may not properly model their interaction (e.g., hydration). A major uncertainty in the latter approach is the user-applied assumption on how the energy is partitioned between phases. For example, one may assume that the constituent materials are always in pressure equilibrium (allowing for different temperatures) or that the energy is partitioned proportionally to the compressibility of each material (allowing for different pressures and temperatures). For H_2O ice, the various assumptions for energy partitioning between phases has a significant effect on the calculated volumes of impact-generated melt. Hence, shock compression experiments are required to determine the correct treatment of icy mixtures.

The response of a mixture to a shock wave, including the partition of energy, will depend upon the characteristic length scale in the mixture compared to the shock front thickness. As natural settings have a wide range of length scales and the thickness of an impact-generated shock front increases significantly as the amplitude of the shock wave decreases (Melosh, 2003), we need to understand how to describe the thermodynamics of shock waves in mixtures of all length scales. We propose three principal regimes of interest that divide the thermodynamics of shock wave propagation in a hydrodynamic mixture: (1) the length scales are sufficiently small that pressure and temperature equilibrate immediately behind the shock front; (2) the length scales are such that pressure equilibrates immediately behind the shock front but thermal equilibration requires more time; and (3) the length scales are sufficiently large that the shock wave must reflect multiple times to reach the equilibrium shock pressure between the components.

Propagation of waves in the largest and smallest length scale regimes is well understood. In an icy mixture at the largest length scales, the thermodynamic path in the H_2O component would be similar to a quasi-isentropic "ring-up" experiment (Ogilvie and Duvall, 1983). In a standard ring-up experiment, a layer of lower impedance material is sandwiched between two layers of a higher impedance material; when a shock is driven through one of the higher impedance layers, multiple shock wave reflections within the low impedance material bring it into pressure equilibrium. For the smallest length scales, Duvall et al. (1971) derived the thermodynamic properties of a two-component mixture in which pressure and temperature equilibrium is achieved behind the shock front. The difference between quasi-isentropic loading (via multiple shock waves) and single shock loading (along a single Rayleigh line) is presented in pressure–volume space in Fig. 1. The increase in internal energy (the *PdV* work) is much less under quasi-isentropic loading compared to a single shock. Therefore, the onset of shock-induced melting of a particular component depends sensitively on the loading path, which is, in turn, dependent on the length scales.

In this work, we focus on understanding the energy partitioning within a mixture in the intermediate length scale regime. Previous experiments have demonstrated that a steady shock wave can propagate in the intermediate length scale regime in many different materials (Holmes and Tsou, 1972; Larson et al., 1973; Zhuang et al., 2003). Consequently, the Rankine–Hugoniot conservation equations for mass, momentum, and energy (Rice et al., 1958) apply to the bulk mixture, and the total internal energy increase is defined. However, the partitioning of energy between the individual phases is not well understood. Duvall et al. (1971) comment that pressure and temperature equilibration is difficult to achieve in a real (rather than ideal) composite because of the much longer time required to reach thermal equilibrium compared to stress equilibrium. Barker (1971) and Munson and Schuler (1971) suggested that the soft component of the mixture will undergo quasi-isentropic loading. In a study considering a wide range of energy partitioning ratios, Krueger and Vreeland (1991) conclude that energy partitioning cannot be determined using measurements of macroscopic shock parameters (shock velocity, particle velocity, pressure, and density) because the amplitude of the difference in the thermal pressure from each component is within the uncertainties of the experiment.

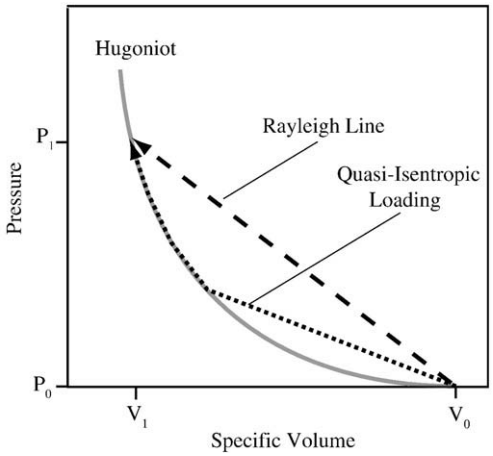

Fig. 1. Schematic of different thermodynamic paths to the same final shock pressure and volume (P_1, V_1) via (1) a single shock wave or (2) multiple shock waves. An ideal single shock wave loads the material along a Rayleigh line, which is the straight line connecting the initial state (P_0, V_0) with the shocked state. If loaded to (P_1, V_1) by means of multiple shock waves, the material is said to follow a quasi-isentropic path. The increase in internal energy is the area under the thermodynamic path.

If the temperature of the components of a mixture were measured, then the partitioning of shock energy could be derived. In practice, this is difficult. However, for mixtures of ice and rock, ice is usually more compressible than the rock. In general, a more compressible material will reach a higher shock temperature compared to a harder material shocked to the same pressure. Hence, the observed radiance from a shocked ice–rock mixture should be dominated by the ice component.

In this study, we consider an H_2O (ice Ih) and SiO_2 (α-quartz) mixture composed of a particle size that we expect to fall into the intermediate length scale regime. H_2O and SiO_2 are materials of tremendous geologic importance; hence, both are well studied under shock compression (Akins and Ahrens, 2002; Luo et al., 2003; Stewart and Ahrens, 2005). The shock and post-shock temperature of pure H_2O ice has been determined experimentally (Stewart et al., 2008). Based on calculations of shock temperature (Wackerle, 1962) and post-shock temperature measurements (Raikes and Ahrens, 1979) for SiO_2, the emission from the SiO_2 component is expected to be much less than from the H_2O component in a mixture.

Here, we present the results from the first shock and post-shock temperature measurements on a H_2O–SiO_2 mixture. Our results are used to make inferences regarding the energy partitioning for the components within intermediate length scale mixtures. We then discuss the implications for calculating the volume of impact-induced melting in the H_2O component of an icy planetary body.

2. Experimental method

Semi-transparent samples were prepared from a 60:40 volumetric mixture of degassed distilled H_2O ice and high purity quartz sand (Mill Creek, OK, No. 1 Dry, U.S. Silica Co.). This volumetric ratio was chosen to minimize porosity in the sample while retaining a significant quartz fraction. The constituent materials were sifted to a particle size of 125 to 250 μm, mechanically mixed, and cold pressed in an evacuated (~1 Pa) piston–die assembly into ~3.0×30.3 mm discs in a 263 K cold room. The bulk density of the samples was $\rho_0 = 1.65 \pm 0.03$ g cm^{-3}. The ice particles were brought to near the melting point during compression to about 5 tons. The flowing ice/

liquid filled the pore space, and upon decompression the sample solidified. The porosity is assumed to be $1.0 \pm 0.5\%$ based on mass balance in similarly prepared samples. In one experiment (18.5 GPa), the sample had a different volumetric ratio of H_2O to SiO_2 (40:60).

The experimental configuration, shown in Fig. 2, was similar to previous simultaneous pyrometry and velocity interferometry experiments on pure H_2O ice (Stewart et al., 2008). The sample was mechanically affixed to an Al-2024 driver plate and encased in a <1 μTorr vacuum chamber with a downrange CaF_2 window. The target assembly was cooled with liquid nitrogen to 108 ± 12 K in order to prevent sublimation of the ice component under vacuum. The downrange free surface velocity was measured using interferometric velocimetry (Barker and Hollenbach, 1972). Emitted radiation was collected downrange and split between two silicon photodiodes (centered at 650 and 810 nm) and a four-wavelength infrared pyrometer (centered at 1.8, 2.3, 3.5, and 4.8 μm) developed by Boboridis et al. (2003) at Los Alamos National Laboratory. The infrared pyrometer is sensitive to radiance at temperatures as low as 300 K with a time resolution of 17 ns. The silicon diodes have a time resolution of 3 ns. The typical error in spectral radiance is 2% at each wavelength.

Planar shock wave experiments were performed by impacting the driver with stainless steel flyer plates accelerated to velocities between 1.2 and 2.7 km s^{-1} using the 40-mm single stage powder gun in the Harvard Shock Compression Laboratory. Projectile velocities were measured immediately prior to impact using three cross-barrel laser diodes. Shock pressures of 7.9 to 22.7 GPa were induced in the sample, which are well above the Hugoniot elastic limits of both ice and quartz.

The experiments are summarized in Table 1. Shock pressures were calculated by the impedance match solution of the release isentrope from the driver and Rayleigh line in the sample (the initial density times the observed shock velocity in the sample). The quoted 1σ error in the shock pressure is based on formal error propagation. Note that the shock pressures are close to those predicted with a mixture Hugoniot derived from a mass average of the pure H_2O and SiO_2 Hugoniots (Meyers, 1994). Other parameters for the impedance match solution and additional experimental details are provided in the Supplemental online materials.

Table 1
Summary of shock temperature experiments in an ice–quartz mixture.

Shock pressure (GPa)	Impact velocity (m/s)	Mixture density (g/cm^3)	Sample thickness (mm)	T_0 (K)	Shock velocity (m/s)
7.9 ± 0.5	1192 ± 7	1.66 ± 0.05	3.09	119	4020 ± 120
12.9 ± 1.1	1725 ± 15	1.67 ± 0.05	2.59	114	4679 ± 259
16.2 ± 1.3	2030 ± 6	1.66 ± 0.04	2.61	109	5102 ± 256
18.5 ± 2.5	2110 ± 30	1.88 ± 0.04	3.05	153	4700 ± 1000
22.7 ± 1.6	2712 ± 7	1.61 ± 0.04	3.34	92	5560 ± 230

Uncertainties are 1σ.

3. Data analysis

Here we present a three-step method to derive the shock temperature of the H_2O component in the H_2O–SiO_2 mixture from the spectral radiance data. First, in Section 3.1.1, we determine the radiation emitted from the shocked layer in a transparent or semi-transparent material. Next, in Section 3.1.2, we introduce a novel method to separate the radiation emitted from the H_2O component from the total radiation from the shocked layer. Then, in Section 3.1.3, we address the effect of shock compressed air, stored in the pore spaces, and fit the individual radiance contributions from air and H_2O. Finally, we describe the post-shock temperature analyses in Section 3.2.

Our analysis relies on the assumptions of a steady wave front and immediate pressure equilibration behind the shock front. Steady shock waves have previously been measured in ice–sand mixtures (Larson et al., 1973). Pressure equilibration is assumed to be achieved based on flat top wave profiles in intermediate length scale mixtures (Dolgoborodov et al., 1992; Larson et al., 1973).

3.1. Shock temperature analysis

3.1.1. Spectral radiance from the shocked layer

As the sample is semi-transparent in the visible and the near-IR wavelengths (0.65, 0.81, 1.8, and 2.3 μm), a method of analysis described by Boslough (1985) and Luo et al. (2004) was used to determine the spectral radiance emitted from the shocked layer, $\epsilon^s L_2$. The spectral radiance observed at the pyrometer, L_0, is fit by

$$L_0 = L_1 e^{-a^s D^s} e^{-a^u D^u} + \epsilon^s L_2 e^{-a^u D^u} \quad (1)$$

at each wavelength. L_1 is the spectral radiance emitted at the driver-sample interface, a^u and a^s are the wavelength-dependent unshocked and shocked absorption coefficients, D^u and D^s are the thicknesses of

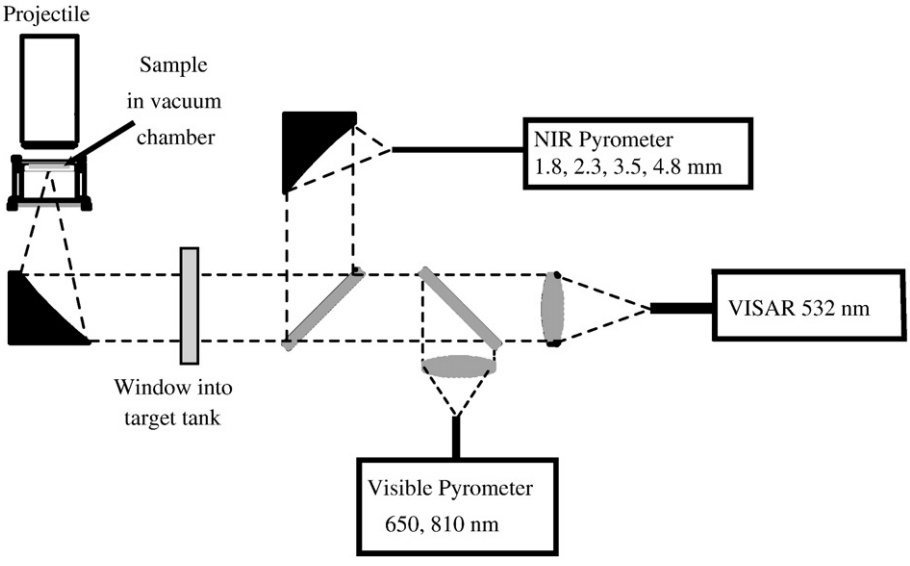

Fig. 2. Plan view of experimental schematic for simultaneous pyrometry and VISAR measurements on the Harvard 40-mm single stage gun.

the unshocked and shocked material, and ϵ^s, the emissivity of the shocked layer, is given by $1-e^{-a^s D^s}$. Throughout this work, superscripts differentiate between shocked 's' and unshocked 'u' material parameters. The fit is performed as a function of time, t, where $D^u = D - U_s t$, $D^s = (U_s - u_p)t$, D is the initial thickness of the sample, U_s is the shock wave velocity (determined from the spectral radiance versus time data, see Fig. 3), and u_p is the particle velocity behind the shock front. Reflectivity is neglected in the analysis based on the low reflectance coefficients determined by the Fresnel Equation.

Representative spectral radiance data are shown in Fig. 3. As Boslough (1985) suggests, the peak in radiance at the start of the data record is likely due to a small amount of air at the interface between the driver and the sample. The radiation from the interface is attenuated as the thickness of strongly absorbing shocked material increases with shock wave propagation. Then, the observed radiation from the shocked layer increases with time as the thickness of unshocked material ahead of the shock front decreases. Spectral radiance data and fits for the other experiments are provided in the Supplemental materials.

For a single-component sample, ϵ^s is the emissivity of the shocked layer and L_2 is the blackbody radiation from the shocked layer. L_2 can then be used to determine the apparent temperature, T_{ap}, of the shocked layer using Planck's Law. T_{ap} is an idealized temperature assuming a perfect blackbody source. The fitted values in Eq. (1) and T_{ap} for each wavelength are provided in Table 2. For the 7.9, 12.9, and 16.2 GPa experiments, typical errors in T_{ap} are about 100 K in the shorter wavelengths and 15 K in the two longer wavelength channels. For the 22.7 GPa experiment, the error in the short wavelength channels are about 30 K, and the error in the longer wavelength channels are about 20 K. For the 18.5 GPa experiment, the radiance from the shock front was not derived as the detectors were saturated.

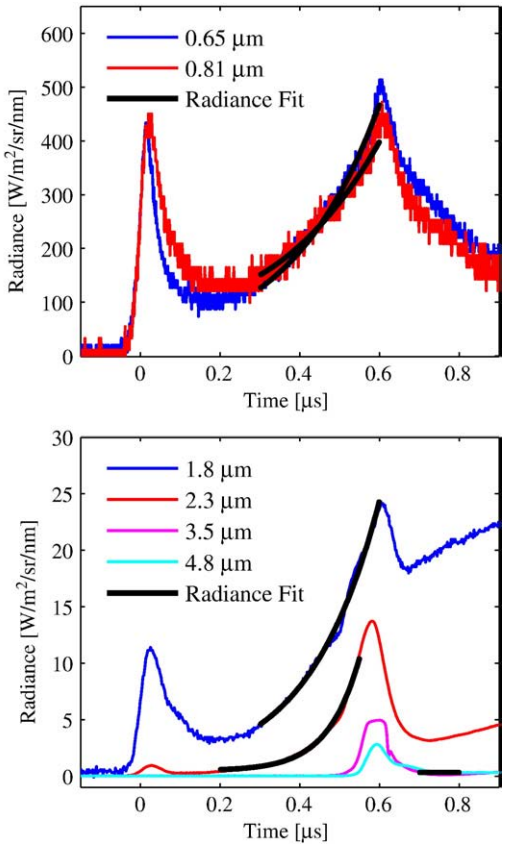

Fig. 3. Spectral radiance emitted from a mixture of H_2O and SiO_2 subjected to a 22.7 GPa planar shock wave. For 0.65, 0.81, 1.8, and 2.3 μm, black lines are fits using Eq. (1). For 3.5 and 4.8 μm, black lines denote time interval used to determine post-shock temperatures.

Table 2
Apparent shock temperatures, T_{ap}, and fitted parameters are determined using Eq. (1) at 0.65, 0.81, 1.8, and 2.3 μm.

Pressure (GPa)	Wavelength (μm)	a_s (m^{-1})	a_u (m^{-1})	L_1 (W/m²/sr/m)	$\epsilon^s L_2$ (W/m²/sr/m)	T_{ap} (K)	T_H (K)
7.9	0.65	1060	971	2.45×10^{11}	4.80×10^{10}	2220	2221
	0.81	1063	672	1.25×10^{11}	4.87×10^{10}	2006	2007
	1.80	3290	960	1.50×10^{10}	2.16×10^{9}	1003	1009
	2.30	3915	1632	1.89×10^{10}	8.49×10^{8}	813	824
Post shock	*3.50*	–	–	–	*6.28×10^{6}*	*391*	*393*
	4.80	–	–	–	*4.87×10^{6}*	*326*	*332*
12.9	0.65	4020	270	4.99×10^{11}	1.35×10^{11}	2476	2479
	0.81	2797	10	5.82×10^{11}	1.79×10^{11}	2351	2353
	1.80	3295	341	6.87×10^{10}	9.2×10^{9}	1224	1232
	2.30	5137	2604	6.28×10^{9}	4.02×10^{9}	1021	1029
Post shock	*3.50*	–	–	–	*1.06×10^{8}*	*536*	*539*
	4.80	–	–	–	*1.41×10^{8}*	*517*	*528*
16.2	0.65	3090	229	8.63×10^{11}	1.66×10^{11}	2536	2538
	0.81	2279	62	6.88×10^{11}	1.77×10^{11}	2348	2350
	1.80	3860	630	2.15×10^{11}	9.30×10^{9}	1227	1229
	2.30	9153	1933	9.90×10^{11}	4.38×10^{9}	1035	1044
Post shock	*3.50*	–	–	–	*3.34×10^{8}*	*631*	*631*
	4.80	–	–	–	*3.07×10^{8}*	*597*	*611*
Post shock (18.5)	*3.50*	–	–	–	*3.86×10^{8}*	*644*	*650*
	4.80	–	–	–	*4.84×10^{8}*	*657*	*679*
22.7	0.65	8830	701	4.79×10^{12}	4.70×10^{11}	2879	2881
	0.81	6467	591	4.38×10^{12}	4.00×10^{11}	2632	2634
	1.80	8070	1010	4.20×10^{11}	2.45×10^{10}	1441	1450
	2.30	4460	2230	1.05×10^{12}	1.92×10^{10}	1373	1379
Post shock	*3.50*	–	–	–	*4.01×10^{8}*	*648*	*652*
	4.80	–	–	–	*2.92×10^{8}*	*591*	*605*

Post-shock radiances and apparent post-shock temperatures, tabulated in italics, are determined at 3.5 and 4.8 μm (Section 3.2). T_H denotes an idealized intermediate temperature inferred for H_2O after separation from the SiO_2 component (Sections 3.1.2 and 3.2).

3.1.2. Spectral radiance from the H_2O component

Although it has been shown experimentally that pressure equilibrates almost immediately after passage of the shock front for mixtures of similar volume ratio, particle size, and shock front thickness (Dolgoborodov et al., 1992), thermal equilibrium will not be reached immediately. We estimate the time scale for thermal equilibration by conduction (as radiative transport can be neglected). Using coefficients of thermal diffusivity and conductivity for H_2O (Abramson et al., 2001) and SiO_2 (Kieffer et al., 1976) at pressures and temperatures near those in our experiment, we have numerically solved the one-dimensional thermal diffusion equation. For the time scale of our experiments (<1 μs), the diffusion length scale in the ice is ~2 μm in the H_2O and ~6 μm in the SiO_2 (see Supplemental material). Considering that the average particle size is ~180 μm, inter-granular thermal equilibrium is not obtained in the time scale of the experiment.

Seifter and Obst (2007) developed a method to separate the radiation from materials with equal emissivities but different temperatures using spectral radiance data. We have extended their method to determine the temperature of a hot material surrounded by a significantly colder material with different emissivity.

We begin by considering the spectral radiance from the shocked layer, $\epsilon^s L_2$ (determined in the previous section), to be an ideal superposition of radiance from the H_2O and SiO_2 components:

$$\epsilon^s L_2 = \alpha_H^R \epsilon_H^s L_H + \alpha_S^R \epsilon_S^s L_S. \quad (2)$$

For each material, subscripted 'H' for H_2O and 'S' for SiO_2, α^R is the radiative area fraction from the shocked layer, and ϵ^s is the emissivity in the shocked state. We can simplify this equation by comparing the spectral radiance from the shocked SiO_2, using theoretical estimates from Wackerle (1962) and Kleeman and Ahrens (1973), to the total radiance from the shocked layer. The calculated radiance from the

SiO_2 is negligible: <1% at each wavelength and smaller than the precision of the calibration. Therefore, within error, the spectral radiance from the H_2O component in the shocked layer, L_H, is given by

$$L_H = \frac{\epsilon^S L_2}{\alpha_H^R \epsilon_H^S}. \quad (3)$$

The physical area fraction, denoted by superscript 'P', of H_2O in the shocked layer is estimated by the initial area fraction, as material in a planar impact undergoes uniaxial strain. However, the radiative area fraction of H_2O in the shocked layer depends on the opacity of the shocked SiO_2. For example, if shocked SiO_2 has a very low absorption coefficient, the radiative area fraction of the H_2O will be approximately one, as radiation emitted from H_2O grains directly behind SiO_2 grains will be transmitted. From a one dimensional radiative absorption analysis (see Supplemental materials), the difference between the physical area fraction, α_H^P, and the radiative area fraction, α_H^R, of H_2O in the shocked layer is given by

$$\alpha_H^R = \alpha_H^P + \alpha_S^P e^{-a_S^S d_S^S}, \quad (4)$$

where, for shocked SiO_2, a_S^S is the absorption coefficient and d_S^S is the average length of a grain.

From the one-dimensional radiative absorption analysis, we also find that the emissivity of the shocked H_2O is slightly dependent on the SiO_2 absorption,

$$\epsilon_H^S = (1-e^{-a_H^S D_H^S} e^{-a_S^S D_S^S}) \frac{(1-e^{-a_H^S d_H^S})}{(1-e^{-a_H^S d_H^S} e^{-a_S^S d_S^S})}, \quad (5)$$

where D_H^S and D_S^S are the summed linear thicknesses of the shocked H_2O and SiO_2 components in the sample, respectively. One may notice that D_H^S and D_S^S increase as the shock wave propagates through the sample, and consequently the emissivity of the H_2O would be a function of time, complicating the interpretation of Eq. (3). However, for the fits performed with a time-dependent emissivity, we find that the emissivity of the shock front is not well constrained. Hence, the emissivity must be a very weak function of time. The inferred time independence requires the absorption coefficients be sufficiently high such that $(1-e^{-a_H^S D_H^S} e^{-a_S^S D_S^S}) \approx 1$ for all the experiments.

The infrared absorption coefficients of H_2O at the pressures and temperatures reached in our experiments are not well constrained; however, based on shock temperature experiments (Stewart et al., 2008), absorption coefficients for H_2O significantly increase with increasing pressure and temperature. In determining the uncertainty on L_H associated with ϵ_H^S, we set a lower bound on the near-IR absorption coefficients of H_2O at the low temperature, ambient pressure values for ice, 909 and 1770 m^{-1} at 1.8 and 2.3 μm, respectively (Warren, 1984). The exact magnitude of the upper bound is not important as the exponential terms in Eq. (5) associated with H_2O quickly go to zero.

For SiO_2, the absorption coefficients, while in the α-quartz phase, are constrained to within a factor of two of the ambient pressure and temperature values, ~1.0 m^{-1} at 0.65, 0.81, 1.8, and 2.3 μm (Drummond, 1936). The tight constraint is based on visible pyrometry measurements on fused quartz, where a negligible increase in the absorption coefficients was found under shock pressures up to about 30 GPa (Kondo and Ahrens, 1983). Note that the dramatic increase in absorption coefficients at shock pressures above 30 GPa was likely due to the structural phase transition to stishovite. According to Zhugin and Krupnikov (1987), the shock-induced phase transition from α-quartz to stishovite does not begin until 23 GPa. For this reason, we assume the α-quartz grains in our samples do not undergo a phase transition during our experiments. The possibility of a change in SiO_2 absorption in the highest pressure experiment is discussed below.

With these assumptions for the absorption coefficients in H_2O and SiO_2, the results from Eqs. (4) and (5) are used in Eq. (3) to determine the spectral radiance from the shocked H_2O component, L_H, under the assumption of an ideal two-component system. Then, the ideal radiance temperatures of the shocked H_2O component, T_H, are derived from L_H using Planck's law at 0.65, 0.81, 1.8, and 2.3 μm. The results are presented in Table 2. Note that the ideal H_2O radiance temperatures are very close to the apparent temperatures, T_{ap}, the ideal blackbody temperature from the combined spectral radiance of all the components in the shocked layer. In the case of an H_2O–SiO_2 mixture, the presence of SiO_2 has a negligible effect on the radiative area fraction and emissivity of H_2O in the shocked layer, which are both close to 1. Hence, we consider the formal errors on T_H to be the same as quoted above for T_{ap}.

3.1.3. Effect of initial porosity

The ideal radiance temperature of the H_2O component, T_H, is highest at the shortest wavelength and monotonically decreases with increasing wavelength (Table 2). This systematic variation was first observed in post-shock temperature measurements on metals (Seifter and Swift, 2008) and has been explained by the presence of small area fractions of material radiating at significantly higher temperatures, known as "hotspots" (Seifter and Obst, 2007).

The ice–quartz samples have an estimated porosity of 1%. The amount of air trapped in pore spaces was minimized by starting with bubble-free ice and pressing the mixture under vacuum; however, even a small amount of shock compressed air reaches much higher temperatures than shocked ice. The magnitude of the radiance from shocked air cannot be predicted due to the unknown mass of air in the pores.

Following the analysis of Seifter and Obst (2007), we fit T_H as a function of wavelength (from 0.65 to 2.3 μm) with a two-component model representing the H_2O and hotspots of air,

$$T_H = \frac{c_2}{\lambda \ln\left[\left(\frac{1-\alpha_{air}}{e^{c_2/\lambda T_{H_2O}}-1} + \frac{\alpha_{air}}{e^{c_2/\lambda T_{air}}-1}\right)^{-1} + 1\right]}, \quad (6)$$

where $c_2 = hc/k \approx 1.439 \times 10^{-2}$ m K is the second radiation constant, h is Planck's constant, c is the speed of light, and k is Boltzmann's constant. α_{air} is the area fraction of shocked air, T_{air} is the temperature of the shocked air, and T_{H_2O} is the true temperature of the shocked H_2O. The three model variables, α_{air}, T_{air}, and T_{H_2O}, are constrained by four wavelengths using a least squares fit weighted by the uncertainties at each wavelength. The fits for each experiment are presented in Fig. 4 and Table 3. The two-component model is an excellent match to the values for T_H at each wavelength. The tabulated uncertainties are the formal uncertainties on the weighted two-component fit. Note that the area fraction of trapped air is comparable to the estimated porosity in the samples.

3.2. Post-shock temperature analysis

Up to this point, we have not discussed the radiance measurements at 3.5 and 4.8 μm because H_2O is completely opaque at these wavelengths (Warren, 1984). The opacity of H_2O at these wavelengths makes the spectral radiance data suitable for deriving post-shock temperatures as radiation from shocked material will not contaminate the light emitted from the material released from the shock state by wave reflection at the downrange free surface.

The spectral radiance of the released material, L_0, at 3.5 and 4.8 μm is obtained by taking an average of the radiance data for a short time interval after the shock front has reached the free surface (Fig. 3). As in Section 3.1.2, we compare the radiance from shock released quartz (Raikes and Ahrens, 1979) with the post-shock radiance data from the ice–quartz mixture. The radiance contribution from the shock

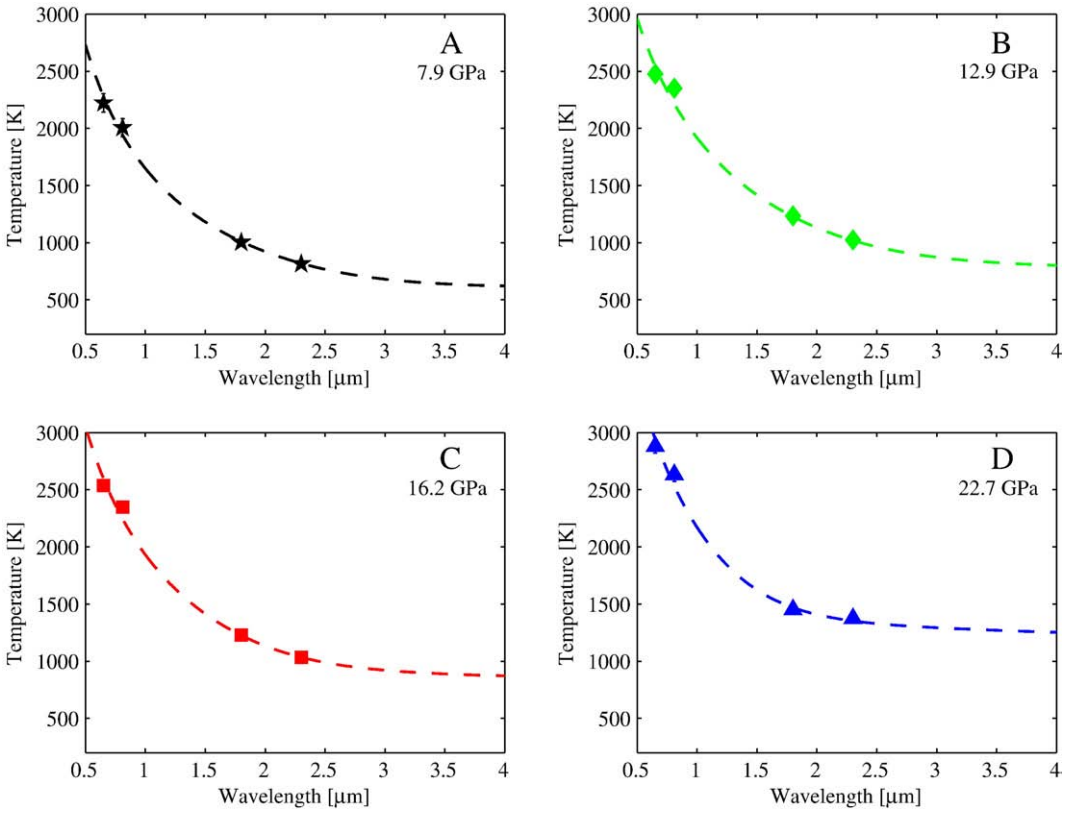

Fig. 4. Two-component (shocked H_2O and shocked air) fits to T_H as a function of wavelength using Eq. (6).

released SiO_2 is negligible at both 3.5 and 4.8 μm. Consequently, we can again simplify our analysis of the post-shock spectral radiance to

$$L_H = \frac{L_0}{\alpha_H^R \epsilon_H}, \tag{7}$$

where L_H is the radiance from the H_2O, α_H^R is the radiative area fraction of the H_2O, and $\epsilon_H \approx 1$ as H_2O is known to be sufficiently opaque at 3.5 and 4.8 μm (Warren, 1984). The reflectivity of the free surface of the sample is negligible (Downing and Williams, 1975), according to the Fresnel Equation.

As in the shock temperature analysis, α_H^R is determined by Eq. (4), where we can again approximate the physical area fractions with their unshocked area fraction. This assumption is reasonable as release is uniaxial for the short period of measurement. At 3.5 and 4.8 μm, the absorption coefficients in SiO_2 are significantly lower than in H_2O: 33 and 950 m^{-1}, respectively (Drummond, 1936). The post-shock radiance temperature of the H_2O component of the mixture is derived from the post-shock radiance, obtained with Eq. (7), using Planck's law. The results are tabulated as T_H in Table 2. The radiance temperature difference between the two wavelengths is small (10 to 60 K); therefore, we infer that the post-shock radiance is negligibly contaminated by released hotspots at the free surface. Hence, we report the true post-shock temperature in H_2O, $T_{H_2O}^{post}$ in Table 3, by the average of the radiance temperatures T_H of H_2O at 3.5 and 4.8 μm. The tabulated uncertainty is from the two-wavelength average.

Table 3
Shock and post-shock temperatures for H_2O.

Shock pressure (GPa)	Shock state			Post-shock state
	α_{air}	T_{air} (K)	T_{H_2O} (K)	T_{H_2O} (K)
7.9	0.001 ± 0.0003	7700 ± 1400	630 ± 140	*360 ± 40*
12.9	0.005 ± 0.002	6500 ± 1100	760 ± 200	*530 ± 10*
16.2	0.004 ± 0.0009	7200 ± 800	850 ± 70	*620 ± 20*
18.5	–	–	–	*660 ± 20*
22.7	0.009 ± 0.003	7700 ± 900	1220 ± 50	*630 ± 30*

Shock state from 2-component analysis, where temperature of shocked air (T_{air}), area fraction of shocked air (α_{air}), and shock temperature of H_2O (T_{H_2O}) are fit using Eq. (6). Post-shock temperatures, tabulated in italics, are the average of the H_2O radiance temperatures at 3.5 and 4.8 μm. Uncertainties are 1σ.

4. Results

In this section, we summarize the shock and post-shock temperature measurements in the context of what is known about the phase diagram and shock response of H_2O. Then, we present information about the shock front thickness from the measurements of free surface velocity. We conclude the section with a discussion of uncertainties.

4.1. Shock temperatures

The H_2O component in the initially ~100 K ice–quartz mixture reaches temperatures between 630 and 1220 K when shocked to pressures between 7.9 and 22.7 GPa (Table 3). The shock temperatures of the H_2O component are plotted in Fig. 5 with a model 100 K principal Hugoniot, quasi-isentrope and principal isentrope. The Hugoniot and isentrope were derived from the 5-Phase H_2O model equation of state (EOS), which is described in detail in the appendix of Senft and Stewart (2008). The quasi-isentrope was constructed by considering a ring-up configuration of H_2O–ice between SiO_2; for a given equilibrium pressure between the two components, the quasi-isentrope temperature is given by the 5-Phase H_2O EOS temperature at the first pressure step.

As shown in Fig. 5, the shock temperatures in the H_2O component are clearly much higher than the principal isentrope and the quasi-

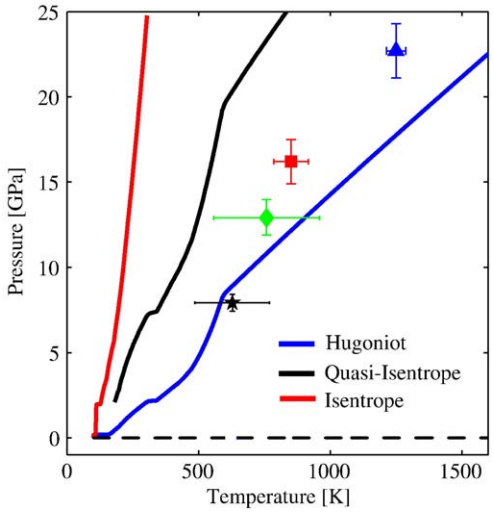

Fig. 5. Shock temperatures in the H_2O component of the mixture (T_{H_2O}, Table 3). Shock states are compared to the model 100 K H_2O ice Hugoniot, quasi-isentrope, and principal isentrope derived from the 5-Phase H_2O EOS (Senft and Stewart, 2008).

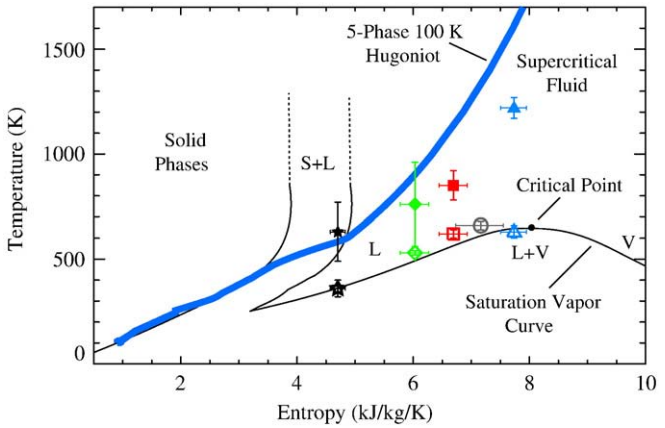

Fig. 6. Simplified temperature–entropy phase diagram for H_2O, with phase boundaries (thin lines) and the 5-Phase model 100 K Hugoniot (thick line). Shock and post shock temperatures in H_2O ice are plotted using the entropy attained by single shock loading to the 5-Phase model Hugoniot (closed and open symbols, respectively).

isentrope. The data points are in agreement with the 5-Phase EOS 100 K principal Hugoniot. The lowest pressure point is in perfect agreement with an experiment in pure H_2O ice: 673 K at 8.2 GPa (Stewart et al., 2008). The shock temperature of the H_2O component at 12.9 GPa (760 ± 200 K) is less than found in pure H_2O shocked to a similar pressure (about 1000 K), but the two agree within 2σ error. The two highest pressure data points are colder than the 5-Phase EOS 100 K principal Hugoniot predicts; however, note that there is no shock temperature data in this pressure regime on pure H_2O ice.

4.2. Post-shock temperatures

The post-shock temperatures in the H_2O component range between 360 and 660 K (Table 3) upon release from shock pressures between 7.9 and 22.7 GPa. Such high temperatures are not expected for full release to ambient pressure. Post-shock temperature measurements by Stewart et al. (2008) revealed that pure H_2O shocked to supercritical fluid initially releases to the saturation vapor curve because full decompression cannot occur until volume expansion allows for production of low-density vapor. On the time scale of the experiments presented here, full decompression is not achieved.

The release to the saturation vapor curve is intuitively presented in temperature–entropy (T–S) space because unloading from the shock state is isentropic and follows a vertical line downward. In Fig. 6, the shock and post-shock temperatures of the H_2O component (filled and open symbols, respectively) are plotted versus the entropy on the principal Hugoniot derived from the 5-Phase H_2O model. The measured post-shock temperatures are in excellent agreement with the saturation vapor temperature at the assumed principal Hugoniot entropy. The temperature and entropy on the saturation vapor curve are very well established (Wagner and Pruss, 2002). Hence, the post-shock temperatures strongly constrain the entropy attained in the shock state. The entropy indicates that the H_2O component reached a state close to the principal Hugoniot at the pressure defined by the bulk impedance of the mixture.

4.3. Free surface particle velocities

The thickness of the shock front can be constrained by the rise time of the shock breakout at the downrange free surface. VISAR measurements of the free surface velocity are presented in Fig. 7 for the 7.9 and 22.7 GPa experiments. Using the shock velocity determined from the radiance measurements (Table 1), the rise times indicate shock front thicknesses of about 220 and 60 μm for the lowest and highest pressure experiments, respectively. As the thickness of the shock front is comparable to or larger than the grain size in the H_2O–SiO_2 mixture, the shock wave is unable to reflect and/or interact multiple times with a single grain before the final shock pressure is achieved. Thus, according to the general classifications presented in the introduction, these experiments fall into the intermediate length scale regime.

4.4. Uncertainties

The tabulated uncertainties for the shock temperature of the H_2O component are formal errors based on the least squares fit using the two-component model (Table 3). Note that high radiance temperatures due to trapped air were also observed in the visible in the shock experiments on pure H_2O ice; however, the relative contribution to the radiance at 1.8 μm and 2.3 μm was significantly less in the pure H_2O experiments because of the differences in sample preparation.

The high radiance in the visible also raises the possibility of nonthermal emission. For example, shock-induced luminescence has been observed in α-quartz at shorter wavelengths than used in this

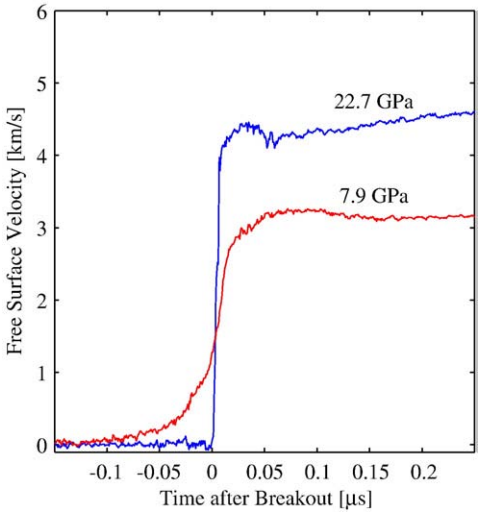

Fig. 7. Free surface particle velocities from the 7.9 and 22.7 GPa experiments measured by velocity interferometry (VISAR). Time axis is adjusted to align shock breakout to the midpoint of the rise in particle velocities.

study (Schmitt and Ahrens, 1989). If nonthermal emission contaminated the two shortest wavelengths used here, then the contribution from hotspots (air) to the total radiance would decrease and the true shock temperatures of the H_2O component would increase to contribute a larger fraction of the radiance observed at the two longer wavelengths. However, the goodness of fit between the measurements and the two-component model coupled with the fact that the fitted area fraction of hotspots is comparable to the porosity in the samples leads us to favor trapped air over nonthermal emission. Some amount of trapped air is expected, and it is unlikely that a nonthermal process mimics air in pore spaces so well.

Another source of uncertainty in the shock temperature of the H_2O component is the assumption of transparency of the SiO_2 component over the range of pressures and temperatures reached in these experiments. Between 0.65 and 2.3 μm, the absorption in SiO_2 is orders of magnitude less than in H_2O under ambient conditions. In the visible, low opacity under shock compression is confirmed by experiments on fused quartz (Kondo and Ahrens, 1983), and we assume that low opacity is also preserved under shock at 1.8 and 2.3 μm. The greatest uncertainty in the opacity of shocked SiO_2 occurs in the highest pressure experiment where there is the possibility of a phase change to stishovite. In this experiment, if the SiO_2 component were opaque, then the shock temperature of the H_2O component would have to be about 300 K higher to yield the same total radiance. In general, uncertainties in the opacity of SiO_2 and the presence of nonthermal emission lead to a possible underestimate in the true shock temperature of H_2O.

The tabulated uncertainties in the post-shock temperature of the H_2O component assume no contamination from hotspots at the free surface. If there were a small high temperature component, then the H_2O release temperatures would be slightly lower and closer to the radiance temperature at 4.5 μm (a difference of <60 K). The uncertainty in the nonthermal radiation in the shocked SiO_2 has no effect on uncertainty of the post-shock temperatures because of the high opacity of H_2O at the two longest wavelengths. If the assumed radiative area fraction of H_2O were less (e.g., equal to the physical area fraction by an increase in the opacity of SiO_2), then the post-shock temperature of the H_2O component would have to be higher by at most 50 K to achieve the same total radiance. Hence, the post-shock temperatures are extremely robust.

5. Discussion

5.1. Energy partitioning in mixtures

In each H_2O–SiO_2 mixture experiment, all of the parameters required to address the question of energy partitioning were determined. We simultaneously measured the (1) shock velocity in the mixture, (2) the shock front thickness, (3) the shock temperature of the H_2O component, and (4) the post-shock temperature of the H_2O component. The shock pressure of the mixture was derived from the shock velocity and impedance match with the aluminum driver. Because of the low compressibility and low emissivity of α-quartz, the radiation from the shocked SiO_2 was negligible. As a result, the radiance from the shock front was dominated by the H_2O component and trace amounts of air. The wavelength-dependent radiance temperatures from the shock front are very well described by a two-component mixture of shocked H_2O and shocked air. The shock temperatures of the H_2O component are in agreement with the 5-Phase model principal Hugoniot at the shock pressure of the mixture. Upon release to the saturation vapor curve, the post-shock temperatures of the H_2O component are strong evidence for single shock compression of the H_2O.

Our results indicate that in the intermediate length scale regime, each component is shocked to a state close to its principal Hugoniot at the shock pressure determined by the bulk impedance of the mixture. Thus, the energy partitioning immediately behind the shock front is simply approximated by the individual Hugoniots of the components in the mixture.

We interpret the observed energy partitioning in a mixture in the context of the three general regimes described in the Introduction. In the small length scale regime, the characteristic length scale of the mixture must be small enough such that the thermal equilibration time is comparable to the rise time of the shock front. Consequently, the energy partitioning is determined by full thermodynamic equilibrium between the components. In the intermediate length scale regime, the shock front thickness is comparable to the length scale of the mixture, and the thermal equilibration time is longer than the rise time. The components are loaded simultaneously to the shock pressure determined by the bulk impedance of the mixture; and the initial energy partitioning is determined by the principal Hugoniots of the components. In the large length scale regime, the characteristic length scale of the mixture is much larger than the shock front thickness. Hence, the shock front is able to reflect at the component boundaries. Pressure equilibration between the components is achieved by a ring-up loading path, and the energy partitioning is determined by the impedance mismatch between the components.

5.2. Melting ice during planetary impact events

Based on the mixture regimes presented above, we now have a framework for calculating the thermodynamic pathways for planetary impacts onto icy mixtures.

Here, we focused on the importance of the length scale of the mixture and the rise time of the shock front. In order to calculate melting upon release from the shock state, one also needs to know the total duration of the shock.

For intermediate length scales, the components of a mixture may be out of thermal equilibrium immediately behind the shock front. However, the duration of the shock pulse will determine how much heat and entropy is lost from the H_2O, via conduction, before release from the shock state. The unloading pathway is isentropic; hence, the entropy of the unloaded H_2O component in an intermediate mixture will depend on the extent of thermal equilibration.

The criteria for shock-induced melting can be considered in terms of a critical entropy that is needed for melting upon release to ambient pressure (Ahrens and O'Keefe, 1972). The criteria can also be thought of as a critical shock pressure required to increase the entropy to the critical value. However, if any entropy is lost via thermal conduction prior to release, the critical shock pressure for melting on release will increase. For pure H_2O ice, the criteria for shock-induced melting and vaporization is well established (Stewart et al., 2008). If shock release occurs before significant thermal conduction between the components, then the critical shock pressures for melting ice in a mixture is simply the same as for pure ice. However, in cases of significant thermal conduction, the entropy at the time of release must be estimated to determine the higher critical shock pressure required for melting on release.

Therefore, determining the criteria for shock-induced melting requires knowledge of the length scale of the mixture and the duration of the shock pulse. In general, these quantities are not well known in planetary situations. Based on shock wave profiles measured from explosive experiments, the thickness of the shock front at low amplitudes is large (up to 100s of meters) and potentially resolvable in numerical simulations (Melosh, 2003). At present, detailed modeling of the initial unequilibrated state and subsequent thermal equilibration in a mixture is not a feature in hydrocodes used for planetary impact events. Hence, hydrocode results will have to be interpreted based on assumptions of mixing lengths and time scales to derive the volumes of melt in a mixture.

This work has demonstrated that in some cases, the volumes of melting in a mixture may be calculated using the criteria for pure H_2O. Details of the volume of melting under different length and time

scales is the subject of future work. Future work will also consider the effects of varying the mixture ratio and the role of strength in the matrix of the mixture.

6. Conclusions

In this work, we address the question of energy partitioning during shock compression of a hydrodynamic material mixture. We construct a conceptual framework to delineate between the different general thermodynamic regimes that are denoted by the ratio of the length scale of the mixture to the thickness of the shock front.

Specifically, we focus on shock-induced melting of H_2O ice in an ice–quartz mixture at intermediate length scales. We performed shock and post-shock temperature experiments and simultaneously determined the shock pressure and shock front thickness. The results indicate that the H_2O ice component was shocked to the principal Hugoniot in the regime where the shock front is comparable to the length scale of the mixture. Hence, the energy partitioning immediately behind the shock front in the intermediate length scale regime is determined by the Hugoniots of the components. In some planetary situations and in these laboratory experiments, release from the shock state occurs before significant heat is lost to the SiO_2 via conduction. In these situations, the critical shock pressures required to melt ice are the same as for pure ice.

In some cases, the length scale of the mixture and the duration of the shock pulse allow for significant thermal conduction between the components before isentropic release to ambient pressures. In these cases, the shock pressures required to melt ice in a mixture will be higher than in pure ice. At present, numerical simulations of impacts onto icy mixtures are not able to capture the complexity of the problem, and educated assessments of length and time scales are needed to infer the amount of melting. This work illustrates the richness and challenges that underlie the deceptively simple question: How much ice melts in a planetary impact event?

Acknowledgments

We thank two anonymous reviewers, Neil Holmes, David Holtkamp, and William Nellis for their insightful comments and conversations. We acknowledge support from DOE NNSA SSGF (grant number DE-FC52-08NA28752) and NASA (grant number NNX06AC13G). We also thank Lee Farina and Sonya Mollinger for their technical assistance.

Appendix A. Supplementary data

Supplementary data associated with this article can be found, in the online version, at doi:10.1016/j.epsl.2009.11.002.

References

Abramson, E., Brown, J., Slutsky, L., 2001. The thermal diffusivity of water at high pressures and temperatures. J. Chem. Phys. 115 (22), 10461–10463. doi:10.1063/1.1418244.
Ahrens, T.J., O'Keefe, J.D., 1972. Shock melting and vaporization of lunar rocks and minerals. Moon 4, 214–249.
Akins, J.A., Ahrens, T.J., 2002. Dynamic compression of SiO_2: a new interpretation. GRL 29 (10), 1394. doi:10.1029/2002GL014806.
Artemieva, N., Lunine, J., 2003. Cratering on Titan: impact melt, ejecta, and the fate of surface organics. Icarus 164 (2), 471–480.
Barker, L., Hollenbach, R.-E., 1972. Laser interferometer for measuring high velocities of any reflecting surface. J. Appl. Phys. 43, 4669–4675.
Barker, L.M., 1971. A model for stress wave propagation in composite materials. J. Compos. Mater. 5, 140–162.
Boboridis, K., Seifter, A., Obst, A.W., 2003. High-speed infrared pyrometry for surface temperature measurements on shocked solids. VDI-Bericht 1784, 119–126.
Boslough, M.B., 1985. A model for time dependence in shock-induced thermal radiation of light. J. Appl. Phys. 58 (9), 3394–3399. doi:10.1063/1.335756.
Carr, M.H., Crumpler, L.S., Cutts, J.A., Greeley, R., Guest, J.E., Masursky, H., 1977. Martian impact craters and emplacement of the ejecta by surface flow. JGR 82 (28), 4055–4065. doi:10.1029/JS082i028p04055.
Cockell, C.S., Bland, P.A., 2005. The evolutionary and ecological benefits of asteroid and comet impacts. Trends Ecol. Evol. 20 (4), 175–179.
Dolgoborodov, A.Y., Voskoboinkikov, I.M., Tolstov, I.K., Sudarikov, A.V., 1992. Anomalies of the propagation of shock waves in mixtures. Fiz. Goren. Vzryva 28, 106–111.
Downing, H.D., Williams, D., 1975. Optical-constants of water in infrared. JGR 80 (12), 1656–1661. doi:10.1029/JC080i012p01656.
Drummond, D., 1936. The infra-red absorption spectra of quartz and fused silica from 1 to 7.5 μm. II. Experimental results. Proc. R. Soc. Lond., Ser. A 153 (879), 328–339.
Duvall, G., Taylor, S.M. Jr., 1971. Shock parameters in a two component mixture. J. Compos. Mater. 5 (2), 130–139.
Furukawa, Y., Sekine, T., Oba, M., Kakegawa, T., Nakazawa, H., 2009. Biomolecule formation by oceanic impacts on early earth. Nat. Geosci. 2 (1), 62–66. doi:10.1038/ngeo383.
Holmes, B., Tsou, F., 1972. Steady shock waves in composite materials. J. Appl. Phys. 43, 957–961.
Kieffer, S., Getting, I., Kennedy, G., 1976. Experimental determination of the pressure dependence of the thermal diffusivity of teflon, sodium chloride, quartz, and silica. JGR 81 (B17), 3018–3024. doi:10.1029/JB081i017p03018.
Kleeman, J., Ahrens, T., 1973. Shock induced transition of quartz to stishovite. JGR 78, 5954–5960. doi:10.1029/JB078i026p05954.
Kondo, K., Ahrens, T.J., 1983. Heterogeneous shock-induced thermal-radiation in minerals. Phys. Chem. Miner. 9 (3–4), 173–181.
Kraus, R. G., Stewart, S. T., in preparation. Scaling laws for impact induced melting and vaporization of H_2O ice. In prep for GRL.
Krueger, B.R., Vreeland, T., 1991. A Hugoniot theory for solid and powder mixtures. J. Appl. Phys. 69 (2), 710–716.
Larson, D.B., Bearson, G.D., Taylor, J.R., 1973. Shock-wave studies of ice and two frozen soils. Permafrost: The North American Contribution to the Second International Conference. National Academy of Sciences, Washington, D.C, pp. 318–325.
Luo, S.N., Ahrens, T.J., Asimow, P.D., 2003. Polymorphism, superheating, and amorphization of silica upon shock wave loading and release. JGR 108 (B9), 13. doi:10.1029/2002JB002317.
Luo, S.N., Akins, J., Ahrens, T., Asimow, P., 2004. Shock-compressed $MgSiO_3$ glass, enstatite, olivine, and quartz: optical emission, temperatures, and melting. JGR 109 (b5), B05205. doi:10.1029/2003JB002860.
Melosh, H.J., 2003. Shock viscosity and rise time of explosion waves in geologic media. J. Appl. Phys. 94 (7), 4320–4325.
Meyers, M.A., 1994. Dynamic Behavior of Materials. John Wiley and Sons, Inc., New York.
Munson, D., Schuler, K., 1971. Steady wave analysis of wave propagation in laminates and mechanical mixtures. J. Compos. Mater. 5 (3), 286–304.
Ogilvie, K.M., Duvall, G.E., 1983. Shock induced changes in the electronic-spectra of liquid CS_2. J. Chem. Phys. 78 (3), 1077–1087.
Pierazzo, E., Artemieva, N.A., Ivanov, B.A., 2005. Starting conditions for hydrothermal systems underneath Martian craters: hydrocode modeling. In: Kenkmann, T., Hörz, F., Deutsch, A. (Eds.), Large Meteorite Impacts III, Special Paper 384. The Geological Society of America, Boulder, CO, pp. 443–457.
Raikes, S.A., Ahrens, T.J., 1979. Post-shock temperature in minerals. Geophys. J. R. Astron. Soc. 58, 717–747.
Rice, M.H., McQueen, R.G., Walsh, J.M., 1958. Compression of solids by strong shock waves. Solid State Phys. 6, 1–63.
Schmitt, D.R., Ahrens, T.J., 1989. Shock temperatures in silica glass — implications for modes of shock-induced deformation, phase-transformation, and melting with pressure. JGR 94 (B5), 5851–5871. doi:10.1029/JB094iB05p05851.
Segura, T.L., Toon, O.B., Colaprete, A., 2008. Modeling the environmental effects of moderate-sized impacts on Mars. JGR 113 (E11). doi:10.1029/2008JE003147.
Segura, T.L., Toon, O.B., Colaprete, A., Zahnle, K., 2002. Environmental effects of large impacts on Mars. Science 298, 1977–1980.
Seifter, A., Obst, A., 2007. About the proper wavelength for pyrometry on shock physics experiments. Int. J. Thermophys. 28 (3), 934–946. doi:10.1007/s10765-007-0191-1.
Seifter, A., Swift, D.C., 2008. Pyrometric measurement of the temperature of shocked molybdenum. Phys. Rev. B 77 (13), 134104. doi:10.1103/PhysRevB.77.134104.
Senft, L., Stewart, S., 2008. Impact crater formation in icy layered terrains on Mars. MAPS 43 (12), 1993–2013.
Senft, L., Stewart, S. T., submitted for publication. Modeling the morphological diversity of impact craters on icy satellites. Icarus.
Stewart, S., Ahrens, T., 2005. Shock properties of H_2O ice. JGR 110, E03005. doi:10.1029/2004JE002305.
Stewart, S., Seifter, A., Obst, A., 2008. Shocked H_2O ice: thermal emission measurements and the criteria for phase changes during impact events. GRL 35, L23203. doi:10.1029/2008GL035947.
Stewart, S.T., O'Keefe, J.D., Ahrens, T.J., 2004. Impact processing and redistribution of near-surface water on Mars. In: Furnish, M.D., Gupta, Y.M., Forbes, J.W. (Eds.), Shock Compression of Condensed Matter — 2003. American Institute of Physics, Melville, NY, pp. 1484–1487.
Wackerle, J., 1962. Shock-wave compression of quartz. J. Appl. Phys. 33, 922.
Wagner, W., Pruss, A., 2002. The IAPWS formulation 1995 for the thermodynamic properties of ordinary water substance for general and scientific use. J. Phys. Chem. Ref. Data 31 (2), 387–535.
Warren, S., 1984. Optical constants of ice from the ultraviolet to the microwave. Appl. Opt. 23, 1026–1225.
Zhuang, S.M., Ravichandran, G., Grady, D.E.W., 2003. An experimental investigation of shock wave propagation in periodically layered composites. J. Mech. Phys. Solids 51 (2), 245–265.
Zhugin, Y.N., Krupnikov, K.K., 1987. Structural peculiarities of plastic front in quartz in the mixed phase region. In: Kedrinskii, V.K. (Ed.), Proceedings of IUPAP, IUTAM Symposium on Nonlinear Acoustics, pp. 196–200.